

## Supporting Information

### Photocatalytic water oxidation with cobalt-containing tungstobismutates: Tuning the metal core

Fabio Evangelisti, Pierre-Emmanuel Car, Olivier Blacque, and Greta R. Patzke\*

#### Table of Contents

<b>Table S1.</b> Crystallographic data and structural refinements for compounds <b>(1)</b> , <b>(2)</b> and <b>(3)</b> .	S2
<b>Table S2.</b> Selected bond distances for Co/Bi-POM <b>(1)</b> .	S3
<b>Table S3.</b> Selected bond distances for Co/Bi-POM <b>(2)</b> .	S4
<b>Table S4.</b> Selected bond distances for Mn/Bi-POM <b>(3)</b> .	S5
<b>Table S5.</b> BVS calculations for Co/Bi-POM <b>(1)</b> .	S6
<b>Table S6.</b> BVS calculations for Co/Bi-POM <b>(2)</b> .	S6
<b>Table S7.</b> BVS calculations for Mn/Bi-POM <b>(3)</b> .	S6
<b>Figure S1.</b> X-ray powder diffraction pattern of bulk Co/Bi-POM <b>(1)</b> vs. calculated pattern.	S7
<b>Figure S2.</b> X-ray powder diffraction pattern of bulk Co/Bi-POM <b>(2)</b> vs. calculated pattern.	S7
<b>Figure S3.</b> X-ray powder diffraction pattern of bulk Co/Bi-POM <b>(3)</b> vs. calculated pattern.	S8
<b>Figure S4.</b> FT-IR spectra of pristine Co/Bi-POM <b>(1)</b> , Co/Bi-POM <b>(2)</b> and Mn/Bi-POM <b>(3)</b> .	S9
<b>Figure S5.</b> TG analysis of pristine Mn/Bi-POM <b>(3)</b> .	S10
<b>Figure S6.</b> Cyclic voltammogram of Co/Bi-POM <b>(1)</b> in H <sub>2</sub> SO <sub>4</sub> (0.4 M) at pH 3.	S11
<b>Figure S7.</b> Cyclic voltammograms of Co/Bi-POM <b>(1)</b> and Co/Bi-POM <b>(2)</b> .	S11
<b>Figure S8.</b> UV/Vis absorption spectra of Co/Bi-POM <b>(1)</b> and Co/Bi-POM <b>(2)</b> .	S12
<b>Figure S9.</b> UV/Vis absorption spectrum of Mn/Bi-POM <b>(3)</b> .	S13
<b>Figure S10.</b> Clark-electrode kinetics for visible-light-driven O <sub>2</sub> formation with Co/Bi-POM <b>(1)</b> .	S14
<b>Figure S11.</b> O <sub>2</sub> evolution for Co/Bi-POM <b>(1)</b> and Co/Bi-POM <b>(2)</b> .	S14
<b>Figure S12.</b> Representative GC kinetics traces of headspace injection of Co/Bi-POM <b>(1)</b> .	S15
<b>Figure S13.</b> O <sub>2</sub> formation kinetics for Co/Bi-POM <b>(1)</b> .	S15
<b>Table S8.</b> Influence of [Ru(bpy) <sub>3</sub> ]Cl <sub>2</sub> and Na <sub>2</sub> S <sub>2</sub> O <sub>8</sub> on WOC performance of Co/Bi-POM <b>(1)</b> .	S16
<b>Figure S14.</b> Representative GC traces showing inactivity of Co/Bi-POM <b>(2)</b> .	S17
<b>Figure S15.</b> FT-IR spectra of pristine POM <b>(1)</b> vs. POM/PS complexes.	S18
<b>Figure S16.</b> TG curves of pristine Co/Bi-POM <b>(2)</b> and Co/Bi-POM <b>(2)</b> /PS complex.	S18











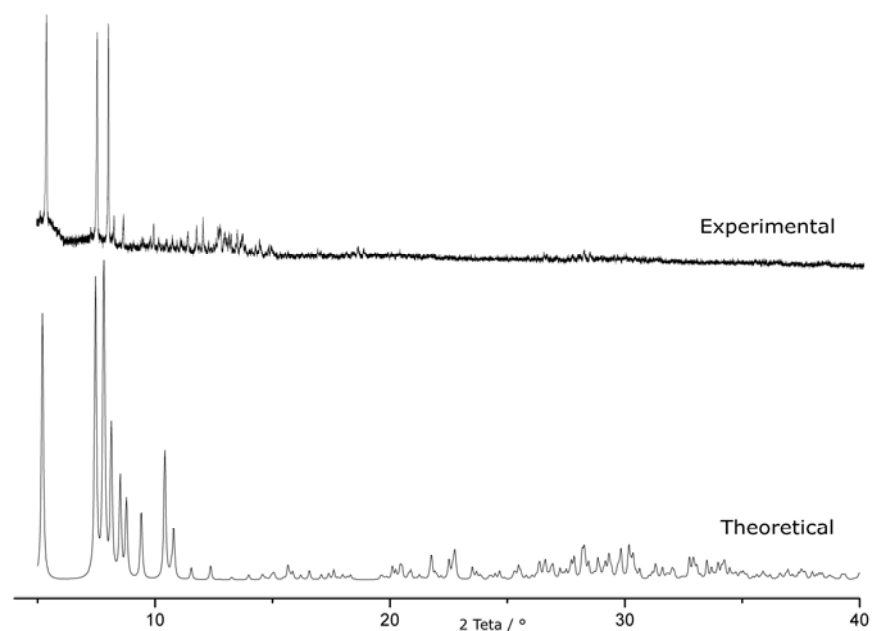


**Figure S1.** X-ray powder diffraction pattern of bulk Co/Bi-POM (**1**) vs. calculated pattern. Intensity differences may be due to preferred orientation of the powder sample.

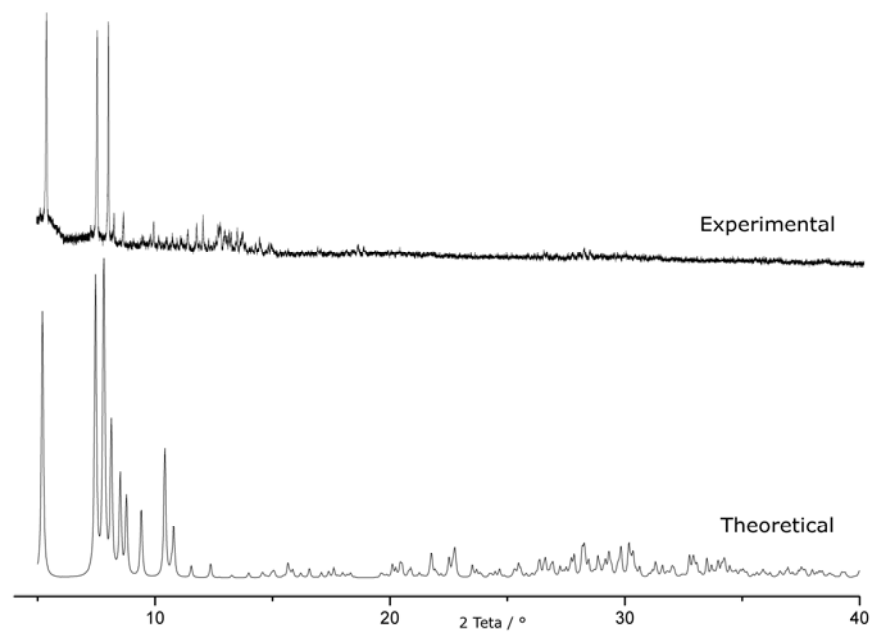


**Figure S2.** X-ray powder diffraction pattern of bulk Co/Bi-POM (**2**) vs. calculated pattern. Intensity differences may be due to preferred orientation of the powder sample.

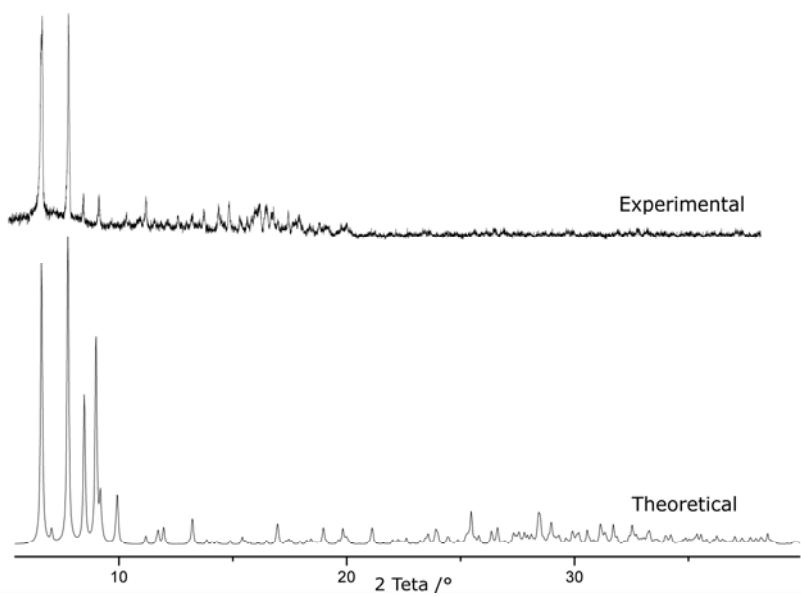


**Figure S3.** X-ray powder diffraction pattern of bulk Co/Bi-POM (**3**) vs. calculated pattern. Intensity differences may be due to preferred orientation of the powder sample.

## 2. Spectroscopic characterization

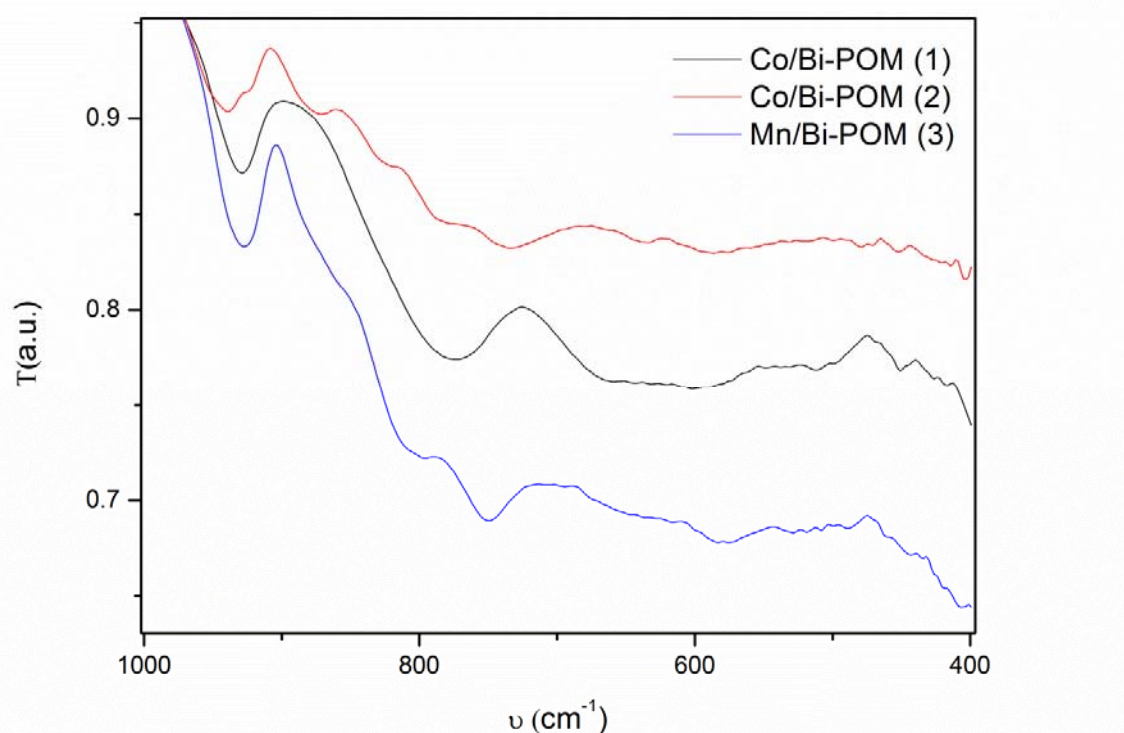


**Figure S4.** FT-IR spectra of pristine Co/Bi-POM (1) (black), Co/Bi-POM (2) (red) and Mn/Bi-POM (3) (blue).

The FT-IR spectrum of Co/Bi-POM (1) (Fig. S4) has one absorption band at 930 cm $^{-1}$  (s) attributed to the characteristic vibration  $\nu$ (W-O(d) stretching), and one broad band centered at 775 cm $^{-1}$  assigned to the  $\nu$ (Co-O-W) stretch vibration of the tetrahedral Co(II) site. The lower energetic and less defined transitions at 664 cm $^{-1}$ , and 425 cm $^{-1}$  are assigned to the  $\nu$ (Co-O-W) stretching vibrations and the 589 cm $^{-1}$  band is assigned to the  $\nu$ (Co-O-W bending) vibration mode.

The FT-IR spectrum of Co/Bi-POM (2) shows differences compared to Co/Bi-POM (1) (see Fig. 4): the vibration bands  $\nu$ (W-O(d) stretch) and  $\nu$ (O(b)-W-O(b) (or W-O-W stretch) are shifted to higher energy (938 cm $^{-1}$  (s) with a shoulder at 953 cm $^{-1}$  (w)), and a series of weak bands appeared at 875 cm $^{-1}$  (s), 823 cm $^{-1}$  (s), 789 cm $^{-1}$  (s) and 733 cm $^{-1}$  (w) assigned to the  $\nu$ (Co-O-W) stretching vibrations.

The FT-IR spectrum of Mn/Bi-POM (3) (Fig. S4) displays one absorption at 926 cm $^{-1}$  (s), another band centered at 870 cm $^{-1}$  (s) and a more defined peak at 759 cm $^{-1}$  (w) attributed to the characteristic vibration bands  $\nu$ (W-O(d) stretching) and  $\nu$ (O(b)-W-O(b) (or W-O-W stretching)). The transition at 578 cm $^{-1}$  (w) is assigned to the  $\nu$ (Mn-O-W) bending of the tetrahedral Mn(II).

### 3. Thermogravimetric analyses (TGA)

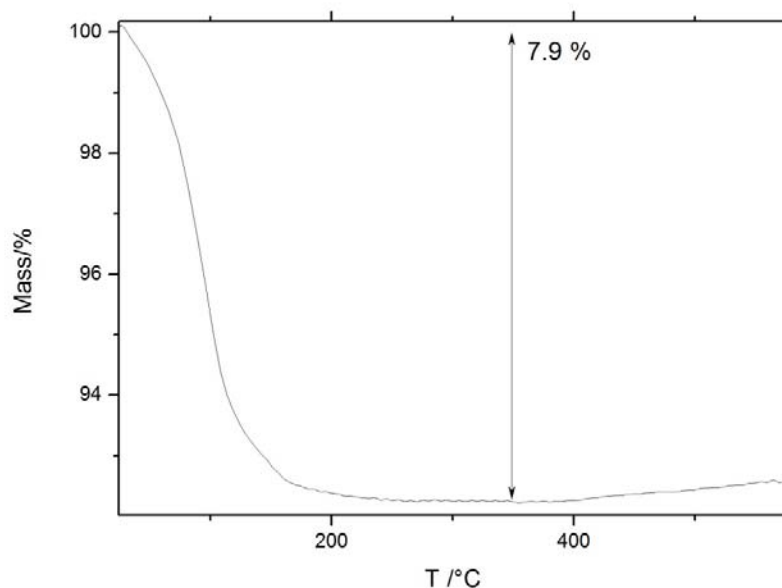


**Figure S5.** TG analysis of pristine Mn/Bi-POM (**3**) (air,  $\text{Al}_2\text{O}_3$  crucible, heating rate 10 K/min).

#### 4. Electrochemical characterization

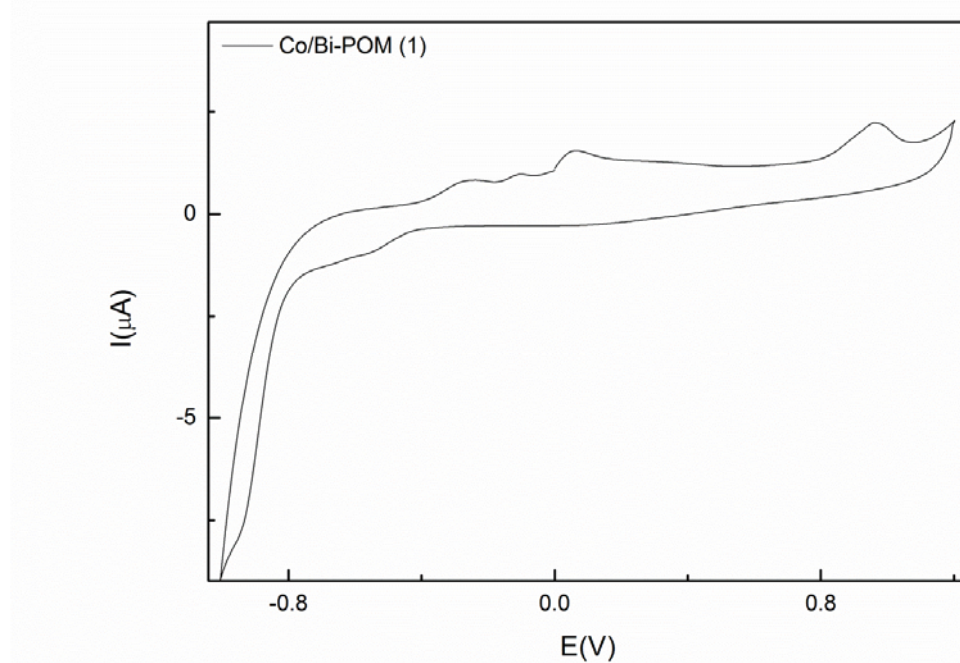


**Figure S6.** Cyclic voltammogram of Co/Bi-POM (1) (15.8 mM) in  $\text{H}_2\text{SO}_4$  (0.4 M) at pH 3 (red line), scan rate: 10 mV/s, (vs. Ag/AgCl).

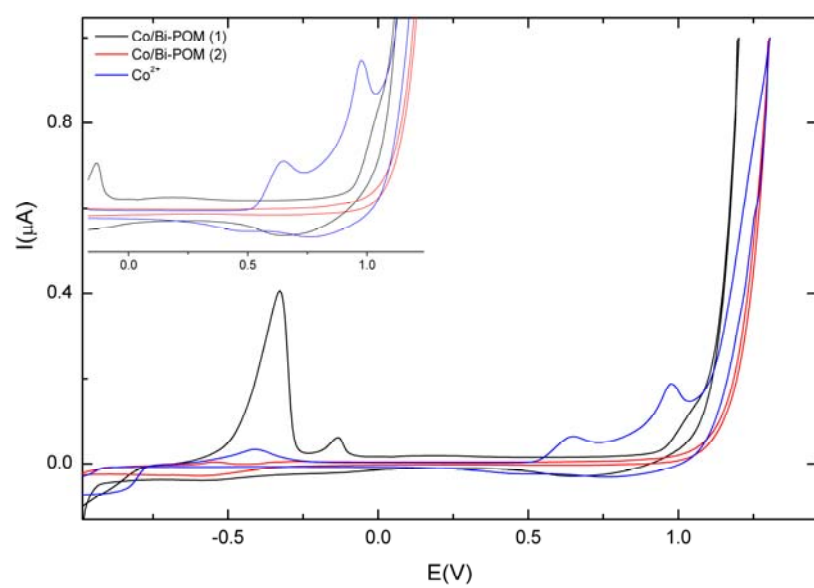


**Figure S7.** Cyclic voltammograms of Co/Bi-POM (1), Co/Bi-POM (2) (both 15.8 mM) and  $\text{Co}(\text{NO}_3)_2$  (50 mM) in  $\text{Na}_2\text{SiF}_6/\text{NaHCO}_3$  buffer (20 mM, pH=5.8); scan rate: 10 mV/s, (vs. Ag/AgCl). Insert: magnification of 0-1 V range.

## 5. Water oxidation catalysis tests

### 5.1. Experimental procedure for WOC activity tests

Water oxidation performance for all compounds has been monitored simultaneously using Clark electrodes and GC equipment. After the degassing process, first 100  $\mu\text{L}$  of headspace were injected into the GC to monitor the efficiency of the He-purging. The  $\text{O}_2/\text{N}_2$  ratio was evaluated and subtracted by the mean of the calibration line. Note that no He-injection in the headspace has been performed in order to re-balance the lower pressure caused by the GC injection.

After evaluation of the purging process, the Clark-electrode was lifted down in the catalytic vial, first in the headspace and once it showed constant voltage, it was moved down into the solution. After 30" of equilibration time at controlled 500 rpm, the irradiation was started and the oxygen evolution kinetics were recorded.

For Co/Bi-POM (**1**), maximum amounts of  $\text{O}_2$  dissolved in solution was obtained after 30 min of Clark electrode monitoring; no GC injection was performed up to this point. GC injection was initiated 1 h after the reaction had started to evaluate the final  $\text{O}_2$  yield of the catalytic process (Fig. S10).

### 5.2. WOC stability tests

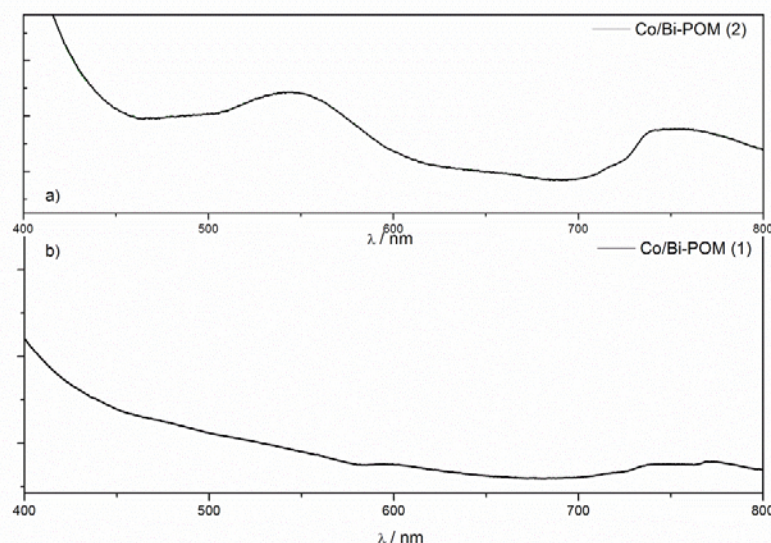


**Figure S8.** UV/Vis absorption spectra of Co/Bi-POM (**1**) (50  $\mu\text{M}$ , bottom) and Co/Bi-POM (**2**) (70 mM, top) in NaPi (40 mM) buffer at pH=8.

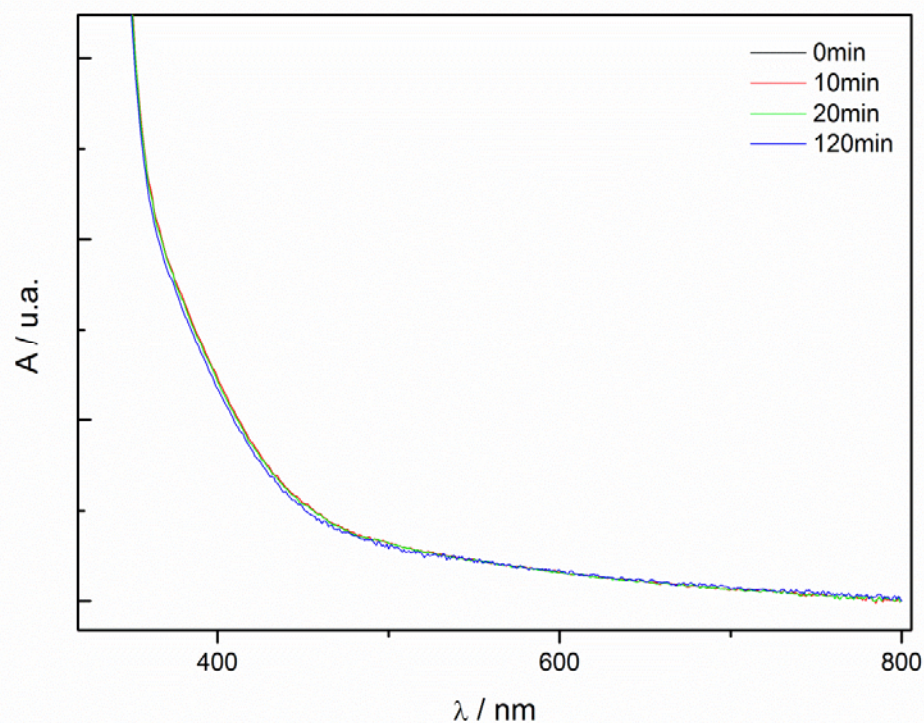


**Figure S9.** UV/Vis absorption spectrum of Mn/Bi-POM (**3**) (50 mM) in  $\text{Na}_2\text{SiF}_6/\text{NaHCO}_3$  buffer (20 mM, pH=5.8).

### 5.3. Clark electrode tests for visible light driven water oxidation

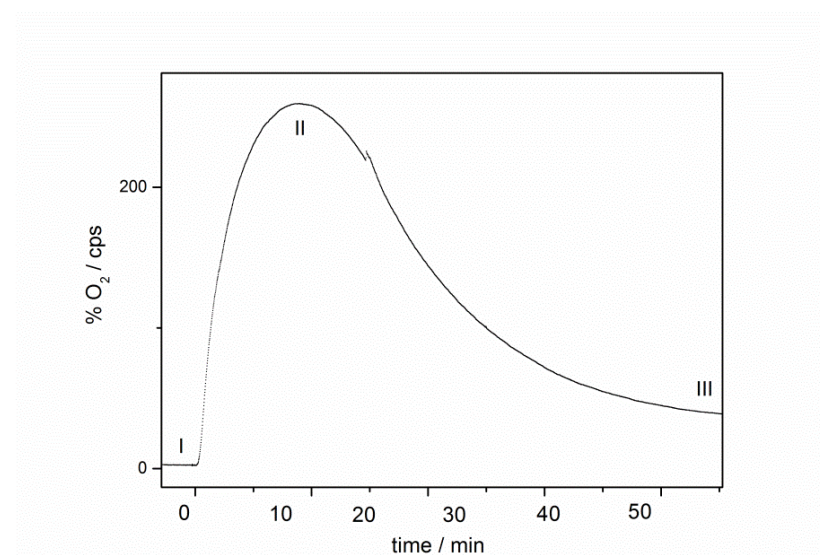


**Figure S10.** Clark-electrode kinetics for visible-light-driven O<sub>2</sub> formation with Co/Bi-POM (**1**). Conditions: LED lamp, 470 nm; 1 mM [Ru(bpy)<sub>3</sub>]Cl<sub>2</sub>, 5 mM Na<sub>2</sub>S<sub>2</sub>O<sub>8</sub>, Na<sub>2</sub>SiF<sub>6</sub>/NaHCO<sub>3</sub> buffer (20 mM, pH=5.8). At time **I** the first GC control-injection is performed, and irradiation was started after complete purging. At time **II**, usually after 20–25 min, the oxygen evolution reached the maximum value after O<sub>2</sub> in solution and headspace were equilibrated, i.e. equilibrium between O<sub>2</sub> (solution) and O<sub>2</sub> (headspace) is reached. The last GC injection was performed after monitoring point **III** with the Clark electrode.

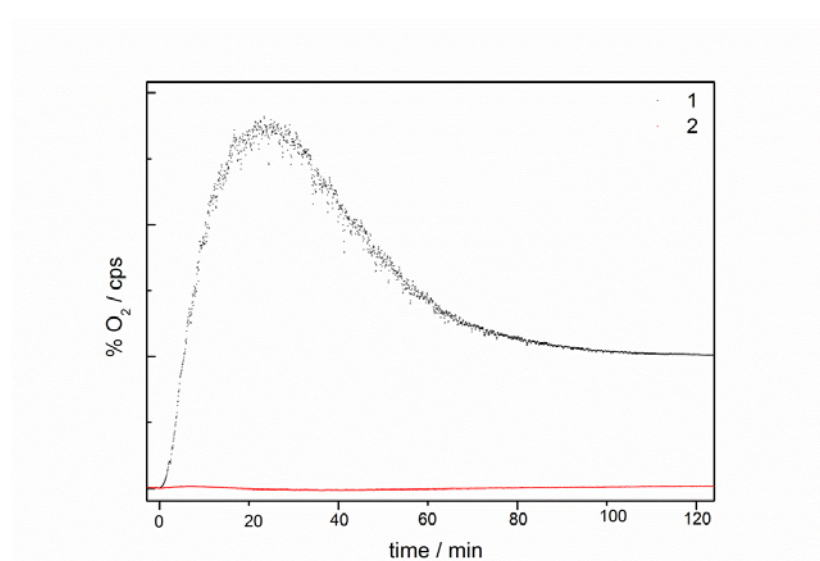


**Figure S11.** Clark-electrode kinetics of visible-light-driven O<sub>2</sub> evolution for Co/Bi-POM (**1**) (black) and Co/Bi-POM (**2**) (red). Conditions: LED lamp, 470 nm; 1 mM [Ru(bpy)<sub>3</sub>]Cl<sub>2</sub>, 5 mM Na<sub>2</sub>S<sub>2</sub>O<sub>8</sub>, Na<sub>2</sub>SiF<sub>6</sub>/NaHCO<sub>3</sub> buffer (20 mM, pH=5.8).

#### 5.4. GC tests for visible-light-driven water oxidation

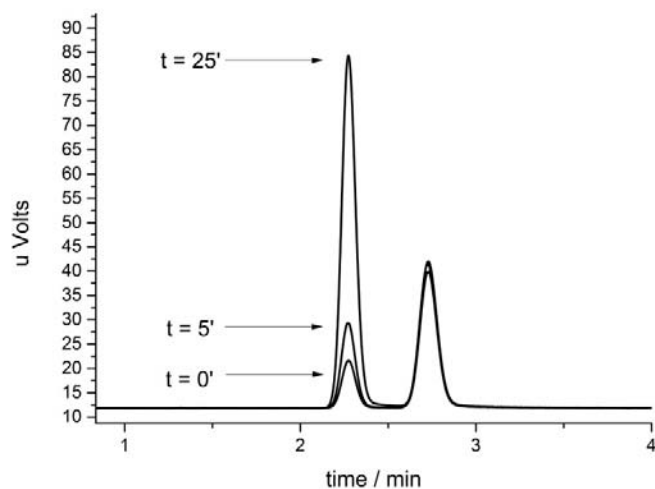


**Figure S12.** Representative GC kinetics traces of headspace injection of Co/Bi-POM (**1**) after 0, 5 and 25 min of illumination with LED lamp, 470 nm (conditions: 1 mM [Ru(bpy)<sub>3</sub>]Cl<sub>2</sub>, 5 mM Na<sub>2</sub>S<sub>2</sub>O<sub>8</sub>, Na<sub>2</sub>SiF<sub>6</sub>/NaHCO<sub>3</sub> buffer (20 mM, pH=5.8)). N<sub>2</sub> area is in line with the manual injection.<sup>1</sup> Referring to Fig. S11, injection at 0 min corresponds to time **I**, injection at 5 min corresponds to a range time between time **I**–**II** and GC injection at 25 min corresponds to a time after **III**.

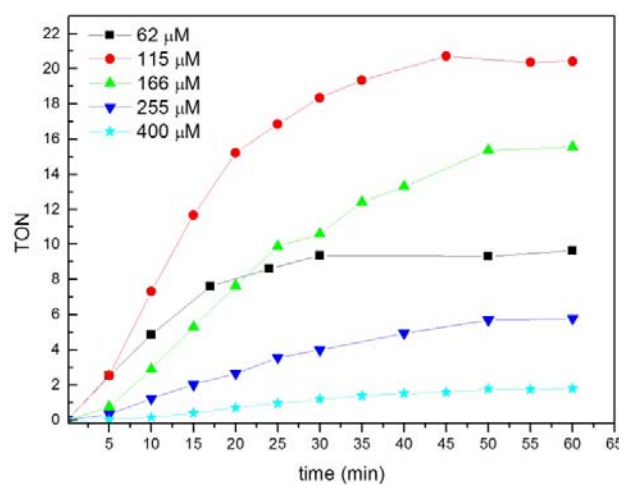


**Figure S13.** GC kinetics for visible-light-driven O<sub>2</sub> formation from water oxidation for Co/Bi-POM (**1**) with persulfate as a sacrificial electron acceptor. Conditions: LED lamp, 470 nm; 1 mM [Ru(bpy)<sub>3</sub>]Cl<sub>2</sub>, 5 mM Na<sub>2</sub>S<sub>2</sub>O<sub>8</sub>, Na<sub>2</sub>SiF<sub>6</sub>/NaHCO<sub>3</sub> buffer (20 mM, pH=5.8). [light blue: 400 μM, black: 62 μM, blue: 255 μM, green: 166 μM, red : 115 μM].

<sup>1</sup> P. E. Car, M. Guttentag, K. K. Baldridge, R. Alberto and G. R. Patzke, *Green Chem.*, 2012, **14**, 1680-1688.

**Table S8.** Influence of  $[\text{Ru}(\text{bpy})_3]\text{Cl}_2$  and  $\text{Na}_2\text{S}_2\text{O}_8$  on WOC performance of Co/Bi-POM (**1**) under different catalytic conditions (top: 1 mM  $[\text{Ru}(\text{bpy})_3]\text{Cl}_2$ , 166  $\mu\text{M}$  (**1**) and different amounts of  $\text{Na}_2\text{S}_2\text{O}_8$  in  $\text{Na}_2\text{SiF}_6/\text{NaHCO}_3$  buffer (20 mM, pH = 5.8).

$\text{NaS}_2\text{O}_8$ (mM)	$\text{O}_2$ ( $\mu\text{mol}$ )	Yield (%)
0	0	0
2	9.2	62.5
5	29.7	96.6
7	21.3	48.3
9	14	23.6

$[\text{Ru}(\text{bpy})_3]\text{Cl}_2$ (mM)	$\text{O}_2$ ( $\mu\text{mol}$ )	Yield (%)
0	0	0
0.5	13.1	40.5
1	28.7	96.6
2	14.4	44.2

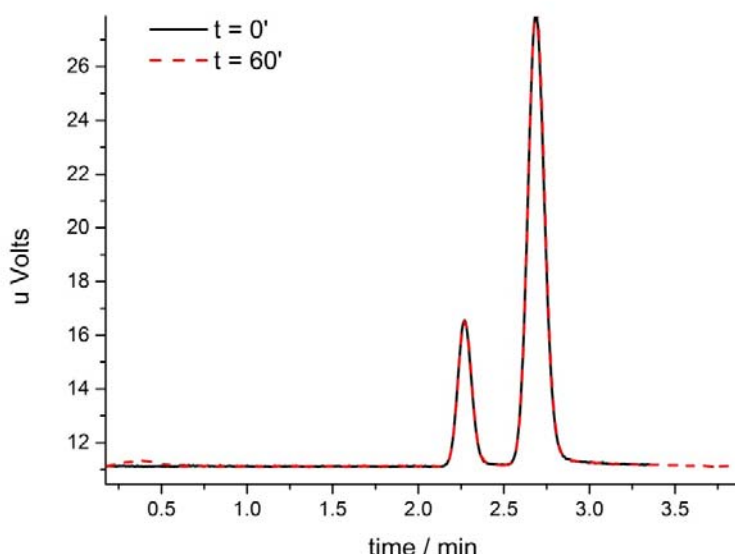


**Figure S14.** Representative GC kinetics traces of headspace injection of Co/Bi-POM (**2**) after 0 and 60 min of irradiation (conditions: 470 nm LED, 1 mM  $[\text{Ru}(\text{bpy})_3]\text{Cl}_2$ , 5 mM  $\text{Na}_2\text{S}_2\text{O}_8$ ,  $\text{Na}_2\text{SiF}_6/\text{NaHCO}_3$  buffer (20 mM, pH = 5.8) and 100  $\mu\text{M}$  of Co/Bi-POM (**2**) as representative concentration).  $\text{N}_2$  area is in line with the manual injection.<sup>2</sup>

<sup>2</sup> P. E. Car, M. Guttentag, K. K. Baldridge, R. Alberto and G. R. Patzke, *Green Chem.*, 2012, **14**, 1680-1688.

### 5.5. Investigation of POM/PS complexes

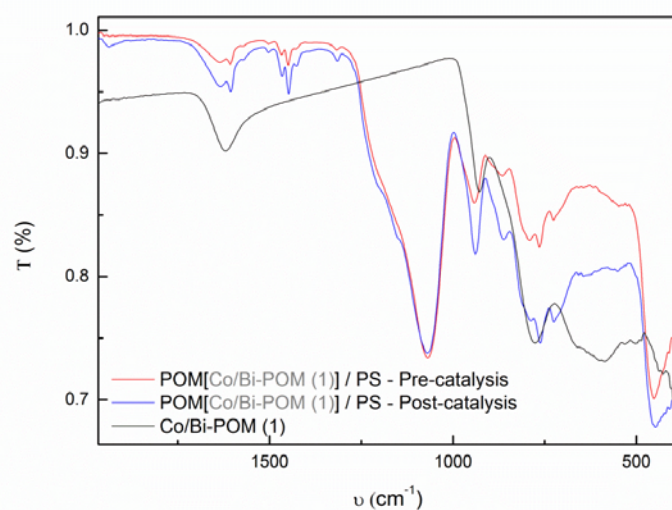


**Figure S15.** FT-IR spectra of of pristine Co/Bi-POM (1) (black), Co/Bi-POM (1)/PS complex obtained from  $\text{Na}_2\text{SiF}_6$  before catalysis (red), Co/Bi-POM (1)/PS complex obtained from  $\text{Na}_2\text{SiF}_6/\text{NaHCO}_3$  buffer (20 mM, pH=5.8) recovered from the second catalytic test (blue).

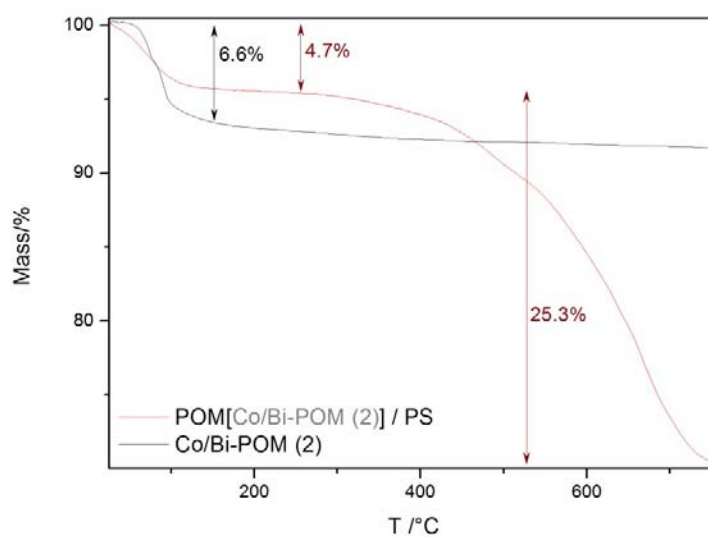


**Figure S16.** TG curves of pristine Co/Bi-POM (2) (black) and Co/Bi-POM (2)/PS complex obtained from  $\text{Na}_2\text{SiF}_6/\text{NaHCO}_3$  buffer (20 mM, pH=5.8) after catalytic test (air,  $\text{Al}_2\text{O}_3$  crucible, heating rate 10 K/min).